

# Pygmalion Effect in Vision: Image-to-Clay Translation for Reflective Geometry Reconstruction

Gayoung Lee<sup>1,2</sup> Junho Kim<sup>1</sup> Jin-Hwa Kim<sup>1,3†</sup> Junmo Kim<sup>2†</sup>

{gayoung.lee, jhkim.ai, jinhwa.kim}@navercorp.com, junmo.kim@kaist.ac.kr

<sup>1</sup>NAVER AI Lab <sup>2</sup>KAIST <sup>3</sup>SNU AIIS

## Abstract

*Understanding reflection remains a long-standing challenge in 3D reconstruction due to the entanglement of appearance and geometry under view-dependent reflections. In this work, we present the Pygmalion Effect in Vision, a novel framework that metaphorically “sculpts” reflective objects into clay-like forms through image-to-clay translation. Inspired by the myth of Pygmalion, our method learns to suppress specular cues while preserving intrinsic geometric consistency, enabling robust reconstruction from multi-view images containing complex reflections. Specifically, we introduce a dual-branch network in which a BRDF-based reflective branch is complemented by a clay-guided branch that stabilizes geometry and refines surface normals. The two branches are trained jointly using the synthesized clay-like images, which provide a neutral, reflection-free supervision signal that complements the reflective views. Experiments on both synthetic and real datasets demonstrate substantial improvement in normal accuracy and mesh completeness over existing reflection-handling methods. Beyond technical gains, our framework reveals that seeing by unshining, translating radiance into neutrality, can serve as a powerful inductive bias for reflective object geometry learning.*

## 1. Introduction

Reconstructing three-dimensional structures from images has long been a fundamental problem in computer vision. The emergence of Neural Radiance Fields (NeRF) [2, 23, 26] marked a major breakthrough in continuous scene representation and photorealistic novel-view synthesis from sparse images. Subsequent studies explored explicit geometry recovery from implicit volumetric representations [1, 37, 41], aiming to bridge neural rendering and mesh-based modeling. More recently, 3D Gaussian Splatting

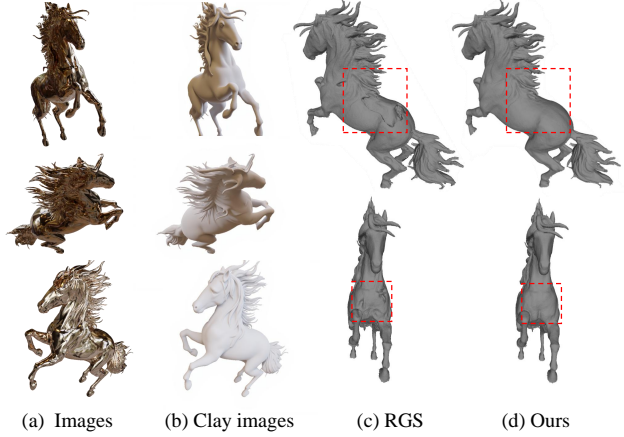


Figure 1. Our method demonstrates that using an image-to-clay model to translate (a) training images into (b) clay images and employing them as geometric guidance in the initial phase leads to improved mesh geometry quality. (c) shows the result of our baseline, Reflective Gaussian Splatting, while (d) presents the result with an additional guidance loss using the clay images.

(3DGS) [14] introduced a point-based differentiable representation that enables real-time, high-fidelity rendering without neural queries at inference. Building upon this direction, 2D Gaussian Splatting (2DGS) [9] collapses the 3D volume into 2D oriented planar Gaussian disks, enabling surface-aligned rendering with higher geometric accuracy.

Despite these advances, reconstructing reflective objects remains a significant challenge. While NeRF- and 3DGS-based models can capture certain non-Lambertian cues, they still implicitly rely on view-invariant radiance consistency, which reflective surfaces violate since their appearance changes with view-dependent environmental reflections. To address this, several inverse-rendering approaches attempt to recover surface reflectance and environment illumination by explicitly modeling specular reflectance parameters within a BRDF formulation [22, 27, 40]. However, jointly optimizing geometry and material properties is chal-

† Co-corresponding authors.

lenging, as appearance and shape are entangled through reflection, making it difficult to attribute observed color variations to either geometry or reflectance.

In contrast to prior works that build increasingly complex models for reflective objects, we reformulate the problem as reconstruction by converting reflective appearances into non-reflective ones using image-to-image translation models. For this conversion, we adopt white clay as the target material. Clay renders, widely used in pipelines such as Blender [3], effectively convey geometric structure without interference from material appearance. This process can be viewed as an instance of the Pygmalion effect in vision (for our analogy, see Sec. A.1), where the model learns to reshape the visual world according to its own learned expectations, turning reflective complexity into a self-consistent, interpretable form. Based on our preliminary experiments, clay-like renderings can be easily synthesized using existing image-to-image translation models without extensive fine-tuning, which we attribute to the abundance of visually similar matte-white objects in real-world image datasets.

Using these clay images, we perform geometry optimization while preserving the existing BRDF estimation framework. To this end, our approach builds upon Reflective Gaussian Splatting [40], which jointly optimizes BRDF parameters of 2D Gaussians. We extend this model by introducing an auxiliary clay color parameter dedicated to generating clay renders that are supervised by the image-to-image-translated clay images. Through additional geometric supervision, our approach achieves more stable training and higher-quality mesh reconstruction, while better disentangling appearance from shape. Experimental results on multiple datasets demonstrate that our method achieves superior mesh quality compared to existing approaches.

In summary, our contributions are as follows:

- A novel framework that uses clay renders from image-to-image translation to enable robust geometry learning for reflective object reconstruction.
- A geometry-guided optimization that supervises rendered clay views for stronger geometric consistency and more stable training.
- Experimental validation demonstrates clear and consistent gains in mesh accuracy and reconstruction stability across multiple reflective object datasets.

## 2. Related work

**Novel-view synthesis with implicit geometry.** Recent advances in novel-view synthesis have been driven by neural implicit representations. NeRF [23] introduced volumetric radiance fields for photorealistic view synthesis, later extended by Mip-NeRF [2] for multiscale anti-aliasing and Instant-NGP [26] for real-time training through hash-grid encoding. Building on this acceleration paradigm, Neurangello [19] and NeuS2 [38] enhanced geometric fidelity

by integrating efficient hash-encoded features into neural surface learning. In parallel, surface-based approaches such as VolSDF [41], UNISURF [28], and MonoSDF [42] explicitly model signed-distance fields or monocular cues to improve geometry reconstruction. More recently, point-based differentiable representations like 3D Gaussian Splatting [14] and 2DGS [9] have achieved real-time rendering with improved geometric consistency.

**Reflective reconstruction.** Reconstructing reflective objects remains challenging due to the entanglement of appearance and geometry under view-dependent reflections. Early attempts such as TensoSDF [18] and NeRO [21] combine volumetric radiance fields with explicit reflectance modeling to jointly learn geometry and BRDF parameters. Recent Gaussian-based approaches address the same issue through differentiable point representations. GShader [13] integrates shading functions into Gaussian splatting for reflective rendering, while GS-IR [20] formulates inverse rendering within the Gaussian domain to estimate reflectance and lighting. R3DG [6] introduces a ray-tracing formulation to better handle high-frequency specular highlights. Further, Ref-GS [43] and RGS [40] focus on disentangling view-dependent radiance from geometry for more accurate reflective reconstruction. GS-2DGS [33] enhances geometric consistency by supervising reflective Gaussians with 2DGS-style depth-regularized rendering. Recent approaches [24, 35] utilize ray-tracing to more accurately model indirect illumination, but this often comes at the expense of substantial computational overhead.

**Image-to-image translation.** Image-to-image translation aims to learn a mapping between visual domains, enabling controllable appearance transformation. Pix2Pix [11] first introduced conditional adversarial learning for paired domain translation, while CycleGAN [44] extended this paradigm to unpaired data using cycle-consistency constraints. Subsequent works such as MUNIT [10] explored multimodal translation with disentangled content and style, and CUT [30] proposed a contrastive objective for more efficient unpaired training. More recently, OminiControl [32] unified spatial and semantic control for flexible image manipulation. These advances inspire ours, where we employ them to convert reflective appearances into diffuse clay-like representations for geometry optimization.

## 3. Method

Our overall framework is visualized in Fig. 2. In Sec. 3.1 and Sec. 3.2, we describe the development of the image-to-clay network for translating images into clay-like images. Subsequently, Sec. 3.3 and Sec. 3.4 present our clay-guided reflective Gaussian splatting method, which utilizes the generated clay images as geometric guidance.

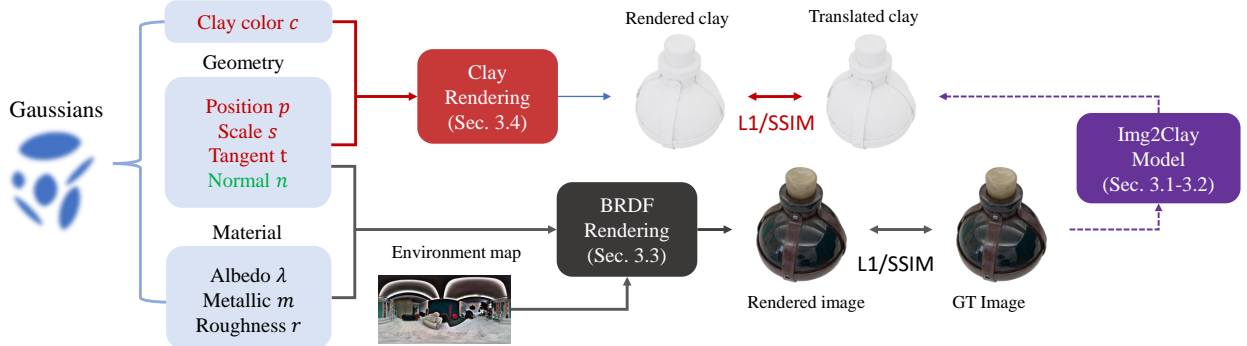


Figure 2. Overview of our dual-branch pipeline. A BRDF-based reflective branch and a clay-guided branch share the same Gaussian geometry. Clay-like images provide reflection-free supervision during early training, stabilizing geometry and improving surface normals.

### 3.1. Image-to-clay translation

To translate reflective surface appearances into diffuse clay-like renderings, we build upon recent progress in image-to-image translation models. Among various architectures, we adopt OminiControl [32], which is based on the FLUX [16, 17] architecture, due to its strong capability in preserving structure while flexibly adapting material appearance. As illustrated in Fig. 3, the model receives noisy image tokens  $\mathbf{X}$ , task description tokens  $\mathbf{C}_T$ , and reflective image tokens  $\mathbf{C}_I$ , which are concatenated into a single unified token sequence  $[\mathbf{X}; \mathbf{C}_T; \mathbf{C}_I]$  to jointly process all modalities through multi-modal attention (MMA), defined over the query  $\mathbf{Q}$ , key  $\mathbf{K}$ , and value  $\mathbf{V}$  tokens as follows:

$$\text{MMA}([\mathbf{X}; \mathbf{C}_T; \mathbf{C}_I]) = \text{softmax} \left( \frac{\mathbf{Q} \mathbf{K}^\top}{\sqrt{d}} + B(\gamma) \right) \mathbf{V}, \quad (1)$$

where  $\gamma$  and  $B(\gamma)$  denote a strength factor and a bias matrix controlling the influence of image and text conditions.

Instead of directly optimizing the large OminiControl backbone, we selectively adapt these lightweight LoRA [8] modules to specialize the model for the image-to-clay translation task. This targeted fine-tuning helps enhance geometric consistency and visual quality of the translated outputs, while mitigating potential side effects when applying auxiliary losses during later joint optimization stages. The red dashed boxes in Fig. 3 indicate the trainable LoRA [8] modules that are fine-tuned using our prepared data, described in the following section.

### 3.2. Data preparation for image-to-clay model

To prepare training data for the image-to-clay translation model, we rendered paired images from Objaverse [4, 5] using Blender with diverse material and lighting conditions. A set of environment maps from PolyHaven [31] was used to introduce realistic illumination variations, and material parameters were systematically perturbed to simulate a wide range of surface appearances. When generating objects with

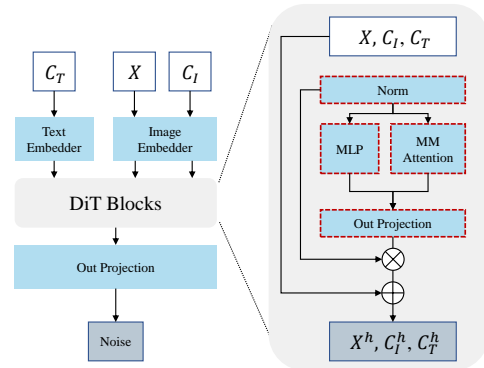


Figure 3. Overall pipeline of the OminiControl model for image-to-clay translation. The red dashed boxes indicate trainable LoRA [8] modules that are fine-tuned (Sec. 3.1).

clay materials, we use the metalness of 0 and the roughness of 1. Example images are shown in Fig. 4. Additional details of the rendering setup are provided in Sec. A.2.

However, embedding Objaverse objects into synthetic environment maps often resulted in unrealistic compositions with limited diversity in background scenes. To overcome these limitations, we additionally constructed realistic image-clay paired data using FLUX [16] and Nano-Banana [7]. Specifically, we first used FLUX to generate clay-style objects, and then used Nano-Banana to convert them into reflective materials. We found that this generation direction yields more stable and visually coherent results than the reverse process, which often introduced artifacts and inconsistent shapes. This asymmetry likely stems from the relative difficulty of mapping complex reflective appearances into diffuse clay-like textures, not a bias in the model toward clay generation. Representative examples of the generated clay and converted reflective images are shown in Fig. 5, and the detailed text prompts are provided in Sec. A.2.



Figure 4. Dataset creation using the Objaverse dataset. The input and GT denote the original reflective and clay-rendered images, respectively, while the output denotes the result from our image-to-clay translation model.

### 3.3. Reflective gaussian splatting

We build upon the Reflective Gaussian Splatting (RGS) [40], where each Gaussian is associated with both geometric and BRDF parameters. Ref-Gaussian adopts the parameterization of 2D Gaussian Splatting (2DGS) [9], which represents each Gaussian on a local tangent plane rather than in 3D volumetric space using  $\mathbf{u}(\mathbf{x})$  for an input  $\mathbf{x}$ . For completeness, a detailed mathematical formulation of 2DGS in our notation is provided in Sec. A.3.

Reflective Gaussian Splatting (RGS) [40] extends each Gaussian to learn physically-based material attributes. Each Gaussian primitive is associated with a feature vector  $\mathbf{b}_i = [\lambda_i, m_i, r_i, \mathbf{n}_i]$ , where  $\lambda_i$ ,  $m_i$ ,  $r_i$ , and  $\mathbf{n}_i$  denote albedo, metallic, roughness, and surface normal, respectively, for the  $i$ -th of  $N$  Gaussians. These attributes are composited using the same alpha blending as in 2DGS:

$$\mathbf{B}(\mathbf{x}) = \sum_{i=1}^N \mathbf{b}_i \alpha_i \hat{\mathcal{G}}_i(\mathbf{u}(\mathbf{x})) \prod_{j=1}^{i-1} \left(1 - \alpha_j \hat{\mathcal{G}}_j(\mathbf{u}(\mathbf{x}))\right), \quad (2)$$

where  $\mathbf{B} = [\Lambda, M, R, \mathbf{N}]$  represents the accumulated material features, while  $\alpha$  and  $\hat{\mathcal{G}}$  denote opacity and 2D Gaussian evaluated at the local tangent coordinate  $\mathbf{u}(\mathbf{x})$ , respectively.

The final outgoing radiance  $L(\omega_o)$  at the viewing direction  $\omega_o$  is computed using the physically-based rendering equation:

$$L(\omega_o) = \int_{\Omega} L_i(\omega_i) f(\omega_i, \omega_o) (\omega_i \cdot \mathbf{N}) d\omega_i, \quad (3)$$

where  $L_i(\omega_i)$  denotes the incoming radiance from direction  $\omega_i$ , and  $f(\omega_i, \omega_o)$  is the bidirectional reflectance distribution function (BRDF).

The BRDF is decomposed into diffuse and specular terms  $f = f_d + f_s$ , while the diffuse term  $f_d$  is straightfor-



Figure 5. Dataset creation using FLUX and Nano-Banana. FLUX (input) images show the synthetic clay objects, Nano-Banana converts them into reflective versions, and the outputs show the reconstructed clay images produced by our model.

ward to integrate, the specular term follows the GGX microfacet model [36]:

$$f_s(\omega_i, \omega_o) = \frac{D G F}{4(\omega_o \cdot \mathbf{N})(\omega_i \cdot \mathbf{N})}, \quad (4)$$

where  $D$ ,  $G$ , and  $F$  denote the normal distribution, geometry, and Fresnel terms, respectively. To efficiently evaluate the specular reflection, we compute the specular radiance  $L_s(\omega_o)$  using the precomputed split-sum formulation:

$$L_s(\omega_o) \approx \left( \int_{\Omega} f_s(\omega_i, \omega_o) (\omega_i \cdot \mathbf{N}) d\omega_i \right) \cdot \left( \int_{\Omega} L_i(\omega_i) D(\omega_i, \omega_o) (\omega_i \cdot \mathbf{N}) d\omega_i \right), \quad (5)$$

where the first term depends only on the view direction and roughness and can therefore be precomputed and stored in a 2D lookup texture, while the second term is efficiently evaluated from prefiltered environment maps.

Following the previous work [40], we further separate the lighting into direct  $L_{\text{dir}}$ , the second term in Eq. (5), and indirect  $L_{\text{ind}}$  components to account for inter-reflection:

$$L'_s(\omega_o) \approx \left( \int_{\Omega} f_s(\omega_i, \omega_o) (\omega_i \cdot \mathbf{N}) d\omega_i \right) \cdot (L_{\text{dir}} \cdot \chi_v + L_{\text{ind}} \cdot (1 - \chi_v)), \quad (6)$$

where  $\chi_v \in \{0, 1\}$  is a binary visibility indicator computed by ray tracing on the extracted mesh surface. The indirect light  $L_{\text{ind}}$  is defined as follows:

$$L_{\text{ind}} = \sum_{i=1}^N l_{\text{ind},i} \alpha_i \prod_{j=1}^{i-1} (1 - \alpha_j), \quad (7)$$

where  $l_{\text{ind},i}$  denotes an additional view-dependent color evaluated along the reflected direction and modeled using spherical harmonics [25].

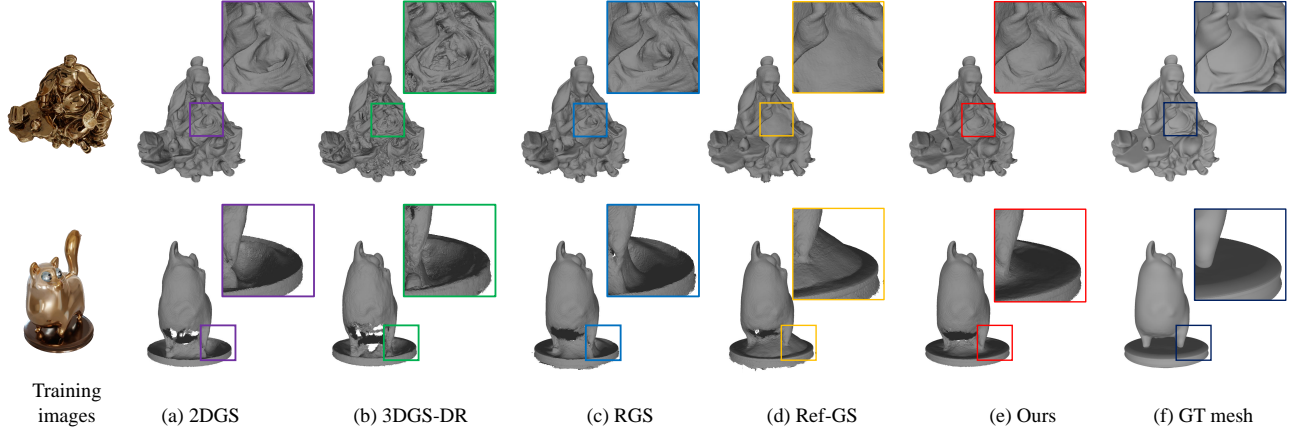


Figure 6. Qualitative comparison on the GlossySynthetic dataset. Our method reconstructs more accurate meshes compared to competing approaches, particularly for regions with complex geometry or strong indirect lights.

### 3.4. Clay-guided reflective Gaussian splatting

In addition to the BRDF-based reflective branch, we introduce an auxiliary branch that renders clay-like images. For this *clay branch*, we additionally introduce a parameter  $\hat{c}_i$  for the clay-like appearance of each Gaussian. Note that both branches operate on the same underlying Gaussian geometry (*i.e.*, position  $\mathbf{p}$ , tangential direction  $\mathbf{t}$ , and scaling factors  $\mathbf{s}$ , and opacity  $\alpha$ ), which facilitates effective multi-task learning.

Unlike the specular branch, the clay branch aims to produce a view-independent appearance. Ideally, the diffuse color should remain constant across viewing directions, and can therefore be easily learned. Then, similar to equation 2, the rendered clay color at pixel  $\mathbf{x}$  can be expressed as:

$$\hat{\mathbf{c}}(\mathbf{x}) = \sum_{i=1}^N \hat{c}_i \alpha_i \hat{\mathcal{G}}_i(\mathbf{u}(\mathbf{x})) \prod_{j=1}^{i-1} \left(1 - \alpha_j \hat{\mathcal{G}}_j(\mathbf{u}(\mathbf{x}))\right). \quad (8)$$

The clay branch is supervised by the pseudo ground-truth clay image  $\mathbf{I}_{\text{clay}}$ , generated by the image-to-clay model, using a combination of  $\mathcal{L}_1$  and SSIM losses:

$$\begin{aligned} \mathcal{L}_{\text{clay}} = & (1 - \lambda_{\text{dssim}}) \|\hat{\mathbf{I}}_{\text{clay}} - \mathbf{I}_{\text{clay}}\|_1 \\ & + \lambda_{\text{dssim}} (1 - \text{SSIM}(\hat{\mathbf{I}}_{\text{clay}}, \mathbf{I}_{\text{clay}})). \end{aligned} \quad (9)$$

Because clay renders contain almost no material texture and exhibit appearance variations mainly due to shading and geometry, we assign a higher SSIM weight  $\lambda_{\text{dssim}} = 0.8$  than in the standard 2DGS formulation.

The total loss is defined as follows:

$$L_{\text{total}} = L_{\text{rgb}} + \lambda_{\text{clay}} L_{\text{clay}}. \quad (10)$$

We train the model with both the original training images and the clay-like images during the early training stage, and

then continue training with the original images only. This schedule is adopted because the clay-like images serve as pseudo ground-truth and may contain reconstruction errors. During training, we jointly optimize the opacity  $\alpha$  and allow gradients from the surface normal  $\mathbf{N}$  to propagate through both the BRDF-based reflective branch and the clay branch.

$$\mathbf{N}_{\text{smooth}} = (1 - \lambda_{\text{smooth}}) \text{sg}(\mathbf{N}) + \lambda_{\text{smooth}} \mathbf{N}, \quad (11)$$

where  $\lambda_{\text{smooth}} = t/T_{\text{clay}}$ , with  $t$  denoting the current iteration and  $T_{\text{clay}}$  the total number of iterations in which clay-like images are used. Here,  $\text{sg}(\cdot)$  denotes the stop-gradient operation. We use  $\mathbf{N}_{\text{clay}}$  in place of  $\mathbf{N}$  in Eq. (5) during the entire clay-training phase for  $t < T_{\text{clay}}$ . This helps the model better handle smooth surface regions that contain limited geometric cues, and enhances the accuracy of surface normals for precise environment-map querying.

In contrast, for  $t < T_{\text{clay}}$ , the remaining geometric parameters are optimized only with the clay-like images by detaching gradients from the BRDF branch. So, the Gaussian positions are predominantly shaped by the clay supervision, while local surface details are refined through color guidance from the original training images, achieving both structural stability and high-fidelity surface reconstruction.

## 4. Experiments

In this section, we compare our method with existing approaches both quantitatively and qualitatively across various datasets to demonstrate its effectiveness. Our method shows notably superior performance in mesh quality, confirming the effectiveness of utilizing clay images for geometry learning.

### 4.1. Implementation details

To train our image-to-clay model, we follow the fine-tuning procedure of OminiControl [32]. The training data consist

Category	Method	Angel	Bell	Cat	Horse	Luyu	Potion	Tbell	Teapot	Avg.	Time (h)
NeRF	TensoSDF [18]	0.0038	0.0066	0.0267	0.0033	0.0083	0.0064	0.0212	0.0085	0.0106	6
	NeRO [21]	0.0034	0.0032	0.0044	0.0049	0.0054	0.0053	0.0035	0.0037	0.0042	12
Gaussian	GShader [13]	0.0060	0.0078	0.0175	0.0072	0.0101	0.0382	0.0308	0.0178	0.0169	0.5
	GS-IR [20]	0.0110	0.1097	0.0566	0.0149	0.0224	0.0593	0.0989	0.0693	0.0553	0.5
	R3DG [6]	0.0090	0.0403	0.0326	0.0117	0.0151	0.0380	0.0472	0.0488	0.0303	1
	Ref-GS [43]	0.0049	0.0084	0.0170	0.0060	0.0098	0.0090	0.0064	0.0084	0.0089	0.7
	RGS [40]	0.0050	0.0071	0.0161	0.0069	0.0093	0.0081	0.0065	0.0090	0.0085	0.6
	GS-2DGS [33]	0.0061	0.0037	0.0074	0.0050	0.0076	0.0088	0.0078	0.0083	0.0068	0.7
	Ours	0.0031	0.0054	0.0082	0.0038	0.0059	0.0073	0.0039	0.0107	0.0061	0.8

Table 1. Chamfer- $\mathcal{L}_1$  ( $\downarrow$ ) distances of 3D reconstruction results on the GlossySynthetic dataset. Rows are grouped by SDF-based and Gaussian-based methods, columns denote test objects, and the rightmost column reports the per-method average. The intensity of the red color signifies a better result.

Method	24	37	40	55	63	65	69	83	97	105	106	110	114	118	122	Avg.
3DGS	2.14	1.53	2.08	1.68	3.49	2.21	1.43	2.07	2.22	1.75	1.79	2.55	1.53	1.52	1.50	1.96
SuGaR	1.47	1.33	1.13	0.61	2.25	1.71	1.15	1.63	1.62	1.07	0.79	2.45	0.98	0.88	0.79	1.33
2DGS	0.48	0.91	0.39	0.39	1.01	0.83	0.81	1.36	1.27	0.76	0.70	1.40	0.40	0.76	0.52	0.80
Ref-GS	0.81	1.20	0.87	0.47	1.39	1.29	0.89	1.23	1.43	0.74	0.76	1.53	0.52	0.96	0.59	0.98
RGS	0.44	0.81	0.31	0.37	1.07	1.15	0.74	1.22	1.17	0.65	0.61	1.26	0.39	0.67	0.52	0.84
Ours	0.48	0.66	0.50	0.38	1.00	0.73	0.60	1.23	1.16	0.63	0.58	1.06	0.40	0.55	0.49	0.74

Table 2. Chamfer- $\mathcal{L}_1$  ( $\downarrow$ ) distances of 3D reconstruction results on the DTU dataset. Columns correspond to the indices of the test objects used in the prior work [9]. The intensity of the red color signifies a better result.

of 100,000 images generated from Objaverse [4] and 5,000 images produced using FLUX [16] and Nano-Banana [7]. To ensure that the Nano-Banana data have an enough influence during training, we sampled the Nano-Banana images five times more frequently than the Objaverse data.

For training our reconstruction model, our method is trained with the clay branch for 10,000 iterations following the procedure described in Sec. 3.4. Afterward, we continued training without the clay branch. We skip the initial training using pure 2DGS since our clay branch makes stable geometry learning without it. All experiments are conducted on a single H100 GPU. The detailed settings are provided in Sec. A.4.

## 4.2. Datasets and metrics

We use four datasets that are widely used for evaluation: two synthetic datasets, Shiny Blender [34] and Glossy Synthetic [21], which render non-Lambertian objects under environment maps, and two real-world datasets, Ref-Real [34] and DTU [12]. Ref-Real contains three real scenes with reflective objects, while DTU includes both reflective and non-reflective objects.

Ground-truth mesh information is available for the Glossy Synthetic and DTU datasets, and mesh quality is assessed using the Chamfer distance computed with the official evaluation code. The photometric quality of novel-view synthesis is also evaluated by comparing rendered results with ground-truth images using PSNR, SSIM, and LPIPS.

## 4.3. Baselines

We compared our method with the various state-of-the-art approaches for reflective object reconstruction. Specifically, we report results from Gaussian-based methods, including GShader [13], GS-IR [20], R3DG [6], RGS [40], GS-2DGS [33], and Ref-GS [43]. For reference, we also include NeRF-based methods such as TensoSDF [18], and NeRO [21].

## 4.4. Comparisons

For quantitative comparison of the generated mesh quality, we measured the Chamfer distance on the GlossySynthetic and DTU datasets, where ground truth meshes are provided. As shown in Tab. 1 and Tab. 2, our method achieves the lowest Chamfer distance for most objects. Qualitative comparisons are provided in Fig. 6 and Fig. 7. As illustrated in Fig. 6, our approach better captures fine geometric details and challenging regions affected by indirect illumination compared to existing methods.

Among existing works, GS-2DGS [33] also uses external normal and depth maps for geometry supervision. However, estimating accurate normals and depths is substantially harder than predicting the grayscale clay images used in our approach. In addition, matte-white images are far easier to obtain with general image-translation models than high-quality depth or normal maps. Overall, our method demonstrates strong performance.

In Tab. 2, we report the Chamfer distance results on

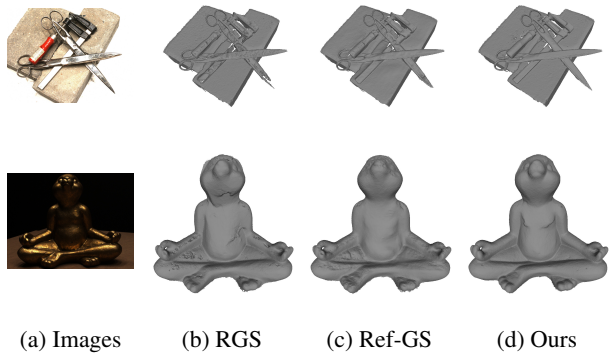


Figure 7. Qualitative comparison of mesh reconstruction results on the DTU dataset. Our method better reconstructs smooth surfaces for reflective objects with rough materials.

the DTU dataset. Unlike GlossySynthetic, DTU contains a mixture of non-reflective and reflective objects, and even for reflective ones with high roughness, recovering a reliable environment map becomes particularly challenging, as shown in Fig. 7. In such cases, methods that rely on BRDFs conditioned on accurately predicted environment maps tend to suffer performance degradation. Our approach remains more robust, as clay-material translation enables optimization independent of the underlying material properties.

We report photometric metrics for novel-view synthesis in Tab. 4. Across datasets, our method achieves competitive photometric performance compared to prior approaches. We visualize the qualitative comparison in Fig. 9. However, our method’s primary strength is not higher RGB fidelity, but markedly improved mesh reconstructions. High-quality geometry extraction is valuable for downstream applications, such as relighting and editing, where accurate surface structure plays a crucial role. Additional result images and visualizations are provided in Sec. A.5.

We report the mean angular error (MAE) of the Shiny Blender dataset [34] in Tab. 3. Although our method shows higher MAE than some baselines, it performs competitively on relatively complex objects such as Toaster, as shown in Fig. 8. This is because, for objects whose geometry can already be easily inferred through BRDF estimation, the relative advantage of our method becomes smaller. As for Coffee, which will be discussed in 4.6, if the image-to-clay model fails to produce a faithful clay translation, our method can exhibit reduced performance. Improving the robustness of the image-to-clay model is a promising direction for future work.

#### 4.5. Ablation studies

To evaluate how effectively the image-to-clay model performs the translation, we conducted experiments with available ground-truth clay renderings. We created a test set of

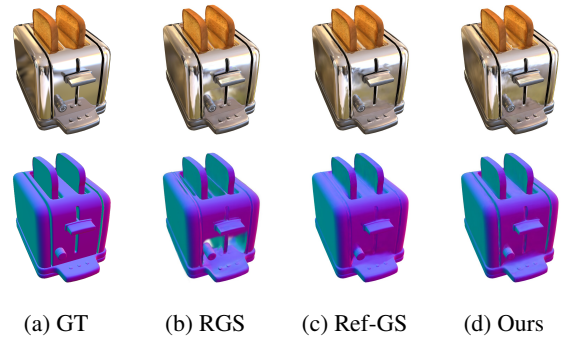


Figure 8. Qualitative comparison on the Shiny Blender dataset: the top row shows RGB renderings, and the bottom row shows surface-normal renderings.

	Car	Ball	Helmet	Teapot	Toaster	Coffee
GS-IR	28.31	25.79	25.58	15.35	33.51	15.38
GShader	14.05	7.03	9.33	7.17	13.08	14.93
3DGS-DR	2.32	0.85	1.67	0.53	6.99	2.21
Ref-GS	2.02	1.05	1.99	0.69	3.92	3.61
RGS	2.27	2.11	2.94	0.70	5.01	3.73
Ours	2.05	1.53	2.40	0.86	3.31	4.50

Table 3. Mean Angular Error of normals on Shiny Blender dataset.

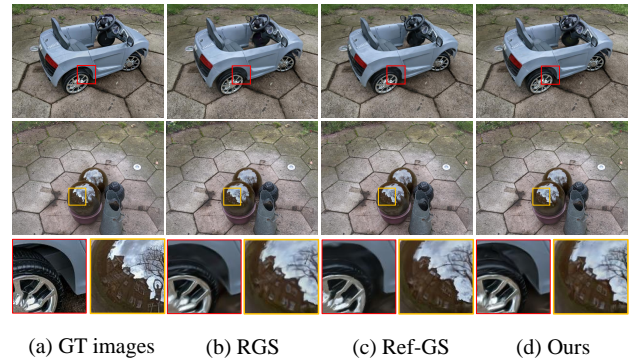


Figure 9. Qualitative comparison of novel-view synthesis results on the Ref-Real dataset. Our method reconstructs the underside of the car and the house windows more sharply.

300 images and compared our model with general image-editing models. The quantitative results are shown in Tab. 5. Qwen-Image-Edit [39] often alters the shape of the given objects. Nano-Banana [7] occasionally shifts the background by several pixels. Since our reconstruction pipeline relies on view consistency, such artifacts pose significant issues. In addition, Fig. 10 shows that the model further fine-tuned with Nano-Banana produces more robust translations on real images while better preserving object shapes.

Next, we conducted an ablation study on the learning strategy for geometry properties in our clay-guided reflective Gaussian splatting framework. As shown in Tab. 6, dur-

Datasets Scenes	Shiny Blender [34]						Glossy Synthetic [21]								Real [34]				
	Ball	Car	Coffee	Helmet	Teapot	Toaster	Angel	Bell	Cat	Horse	Luyu	Potion	Tbell	Teapot	Garden	Sedan	Toycar		
PSNR $\uparrow$																			
2DGS	25.97	26.38	32.31	27.42	44.97	20.42	26.95	24.79	30.65	25.18	26.89	29.50	23.28	21.29	22.53	26.23	23.70		
GShader	30.99	27.96	32.39	28.32	45.86	26.28	25.08	28.07	31.81	26.56	27.18	30.09	24.48	23.58	21.74	24.89	23.76		
R3DG	23.64	25.92	30.10	25.01	43.15	18.80	24.90	23.51	27.59	23.37	24.68	27.29	21.25	20.47	21.92	21.18	22.83		
3DGS-DR	33.43	30.48	34.53	31.44	47.04	26.76	29.07	30.60	32.59	26.17	28.96	32.65	29.03	25.77	21.82	26.32	23.83		
Ref-GS	36.10	30.94	34.38	33.40	46.69	27.28	30.34	31.70	33.15	27.45	29.46	32.64	30.08	26.47	22.48	26.63	24.20		
RGS	37.01	31.04	34.63	32.32	47.16	28.05	30.38	32.86	33.01	27.05	30.04	33.07	29.84	26.68	22.97	26.60	24.27		
Ours	33.83	31.09	29.62	31.32	46.11	28.20	30.39	31.54	33.51	27.64	30.11	31.94	29.74	26.17	23.04	25.82	24.56		
SSIM $\uparrow$																			
2DGS	0.934	0.930	0.972	0.953	0.997	0.892	0.918	0.911	0.958	0.909	0.918	0.939	0.902	0.886	0.609	0.778	0.597		
GShader	0.966	0.932	0.971	0.951	0.996	0.929	0.914	0.919	0.961	0.933	0.914	0.936	0.898	0.901	0.576	0.728	0.637		
R3DG	0.888	0.922	0.963	0.931	0.995	0.858	0.894	0.888	0.934	0.878	0.889	0.911	0.875	0.869	0.556	0.643	0.657		
3DGS-DR	0.979	0.963	0.976	0.971	0.997	0.942	0.942	0.959	0.973	0.933	0.943	0.959	0.958	0.942	0.581	0.773	0.639		
Ref-GS	0.981	0.961	0.973	0.975	0.997	0.950	0.955	0.965	0.973	0.948	0.946	0.957	0.956	0.944	0.607	0.783	0.656		
RGS	0.981	0.964	0.976	0.971	0.998	0.948	0.954	0.969	0.973	0.944	0.952	0.963	0.962	0.947	0.617	0.777	0.660		
Ours	0.976	0.962	0.958	0.964	0.997	0.946	0.954	0.957	0.975	0.950	0.953	0.952	0.961	0.943	0.629	0.771	0.673		
LPIPS $\downarrow$																			
2DGS	0.156	0.052	0.079	0.079	0.008	0.127	0.072	0.109	0.060	0.071	0.066	0.097	0.125	0.101	0.254	0.225	0.396		
GShader	0.121	0.044	0.078	0.074	0.007	0.079	0.082	0.098	0.056	0.062	0.064	0.088	0.091	0.122	0.274	0.259	0.239		
R3DG	0.214	0.058	0.090	0.125	0.013	0.170	0.085	0.125	0.089	0.081	0.080	0.117	0.156	0.115	0.354	0.380	0.312		
3DGS-DR	0.105	0.033	0.076	0.050	0.006	0.082	0.052	0.050	0.042	0.049	0.041	0.046	0.046	0.076	0.073	0.064	0.247	0.208	0.231
Ref-GS	0.098	0.034	0.082	0.045	0.006	0.070	0.042	0.049	0.041	0.046	0.046	0.076	0.073	0.064	0.242	0.196	0.236		
RGS	0.098	0.033	0.076	0.049	0.006	0.074	0.042	0.040	0.040	0.048	0.043	0.064	0.058	0.058	0.256	0.245	0.256		
Ours	0.077	0.034	0.096	0.064	0.008	0.078	0.041	0.052	0.038	0.042	0.041	0.078	0.063	0.058	0.254	0.219	0.255		

Table 4. Per-scene image quality comparison on synthesized test views. The intensity of the red color signifies a better result.

Method	PSNR $\uparrow$	SSIM $\uparrow$	LPIPS $\downarrow$
Qwen-Image-Edit	21.21	0.712	0.292
Nano-Banana	23.87	0.759	0.210
Ours	<b>24.27</b>	<b>0.874</b>	<b>0.192</b>



Table 5. Quantitative comparison of clay-image translation fidelity on test data generated from Objaverse.

Detached for RGB	$N_{\text{smooth}}$	Average CD $\downarrow$
None	yes	0.0069
$p$	yes	0.0064
$p, t, r$	no	0.0063
$p, t, r$	yes	<b>0.0061</b>
$p, t, r, N$	no	0.0078

Table 6. Ablation results examining geometry learning strategies.

ing the early stage, it is beneficial to detach the remaining geometry parameters from the RGB loss. While clay images provide strong guidance for overall shape, they offer limited visual cues on smooth surfaces; therefore, supervising the Gaussian normals using BRDF-based rendering losses helps improve reconstruction quality in such cases. We also show that smoothly increasing the contribution of the RGB loss using  $N_{\text{smooth}}$  is beneficial for better focusing geometry learning in the early stage.

#### 4.6. Limitations

As shown in Fig. 11, incorrect predictions from the image-to-clay model can interfere with geometry learning. The

Figure 10. Effect of incorporating Nano-Banana data for real images: (left) input images, (middle) the results without Nano-Banana data, and (right) the results with Nano-Banana data. The model trained with Nano-Banana data preserves finer details in the hand region of the rabbit sculpture.

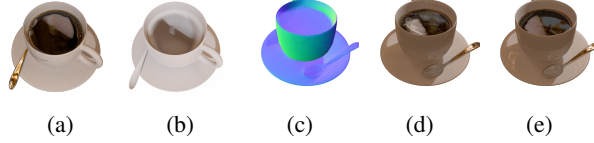


Figure 11. Limitation of our method: incorrect image-to-clay translation can lead to inaccurate geometry learning. (a) training image, (b) translated clay image, (c) predicted normal on a test view, (d) predicted RGB image, and (e) ground-truth image.

coffee inside the mug is not well represented in the training data, causing the model to translate it inaccurately. This inconsistency then disrupts geometry learning and leads to inaccurate reconstruction as shown in (c). Improving the translation model by training it on a broader range of material and lighting conditions would likely further enhance the performance of our method.

## 5. Conclusion

We presented the Pygmalion Effect in Vision, a framework that reconstructs reflective objects by reducing specular ambiguity through clay-guided supervision. Combining a BRDF-based reflective branch with a clay-guided branch using synthesized clay images enables reliable disentanglement of reflection and geometry. Beyond practical gains, our results suggest that neutralizing specular cues offers a strong inductive bias for learning geometry, pointing toward new directions for challenging materials and appearance modeling.

## Acknowledgments

We sincerely appreciate Sangdoo Yun for his valuable support and insightful feedback. The NAVER Smart Machine Learning (NSML) platform [15] was used for the experiments.

## References

- [1] Dejan Azinović, Ricardo Martin-Brualla, Dan B Goldman, Matthias Nießner, and Justus Thies. Neural RGB-D surface reconstruction. In *CVPR*, 2022. 1
- [2] Jonathan T Barron, Ben Mildenhall, Matthew Tancik, Peter Hedman, Ricardo Martin-Brualla, and Pratul P Srinivasan. Mip-NeRF: A multiscale representation for anti-aliasing neural radiance fields. In *ICCV*, 2021. 1, 2
- [3] Blender Online Community. *Blender - a 3D modelling and rendering package*. Blender Foundation, 1994. 2
- [4] Matt Deitke, Dustin Schwenk, Jordi Salvador, Luca Weihs, Oscar Michel, Eli VanderBilt, Ludwig Schmidt, Kiana Ehsani, Aniruddha Kembhavi, and Ali Farhadi. Objaverse: A universe of annotated 3d objects. *arXiv preprint arXiv:2212.08051*, 2022. 3, 6, 11
- [5] Matt Deitke, Ruoshi Liu, Matthew Wallingford, Huong Ngo, Oscar Michel, Aditya Kusupati, Alan Fan, Christian Laforte, Vikram Voleti, Samir Yitzhak Gadre, Eli VanderBilt, Aniruddha Kembhavi, Carl Vondrick, Georgia Gkioxari, Kiana Ehsani, Ludwig Schmidt, and Ali Farhadi. Objaverse-xl: A universe of 10m+ 3d objects. *arXiv preprint arXiv:2307.05663*, 2023. 3, 11
- [6] Jian Gao, Chun Gu, Youtian Lin, Zhihao Li, Hao Zhu, Xun Cao, Li Zhang, and Yao Yao. Relightable 3d gaussians: Realistic point cloud relighting with brdf decomposition and ray tracing. In *ECCV*, 2024. 2, 6, 12
- [7] Google DeepMind. Nano banana image editing in gemini just got a major upgrade. <https://blog.google/products/gemini/updated-image-editing-model/>, 2025. Accessed: 2025-11-05. 3, 6, 7, 12
- [8] Edward J Hu, Yelong Shen, Phillip Wallis, Zeyuan Allen-Zhu, Yuanzhi Li, Shean Wang, Lu Wang, Weizhu Chen, et al. Lora: Low-rank adaptation of large language models. In *ICLR*, 2022. 3
- [9] Binbin Huang, Zehao Yu, Anpei Chen, Andreas Geiger, and Shenghua Gao. 2d gaussian splatting for geometrically accurate radiance fields. In *ACM TOG*, 2024. 1, 2, 4, 6, 11, 12
- [10] Xun Huang, Ming-Yu Liu, Serge Belongie, and Jan Kautz. Multimodal unsupervised image-to-image translation. In *ECCV*, pages 172–189, 2018. 2
- [11] Phillip Isola, Jun-Yan Zhu, Tinghui Zhou, and Alexei A Efros. Image-to-image translation with conditional adversarial networks. In *CVPR*, 2017. 2
- [12] Rasmus Jensen, Anders Dahl, George Vogiatzis, Engin Tola, and Henrik Aanæs. Large scale multi-view stereopsis evaluation. In *CVPR*, 2014. 6
- [13] Yingwenqi Jiang, Jiadong Tu, Yuan Liu, Xifeng Gao, Xiaoxiao Long, Wenping Wang, and Yuexin Ma. GaussianShader: 3d gaussian splatting with shading functions for reflective surfaces. In *CVPR*, 2024. 2, 6
- [14] Bernhard Kerbl, Georgios Kopanas, Thomas Leimkühler, and George Drettakis. 3d gaussian splatting for real-time radiance field rendering. *ACM TOG*, 2023. 1, 2
- [15] Hanjoo Kim, Minkyu Kim, Dongjoo Seo, Jinwoong Kim, Heungseok Park, Soeun Park, Hyunwoo Jo, KyungHyun Kim, Youngil Yang, Youngkwan Kim, Nako Sung, and Jung-Woo Ha. NSML: Meet the MLAAS platform with a real-world case study. *arXiv preprint arXiv:1810.09957*, 2018. 9
- [16] Black Forest Labs. Flux. <https://github.com/black-forest-labs/flux>, 2024. 3, 6, 12
- [17] Black Forest Labs, Stephen Batifol, Andreas Blattmann, Frederic Boesel, Saksham Consul, Cyril Diagne, Tim Dockhorn, Jack English, Zion English, Patrick Esser, Sumith Kulal, Kyle Lacey, Yam Levi, Cheng Li, Dominik Lorenz, Jonas Müller, Dustin Podell, Robin Rombach, Harry Saini, Axel Sauer, and Luke Smith. Flux.1 kontext: Flow matching for in-context image generation and editing in latent space. *arXiv preprint arXiv:2506.15742*, 2025. 3
- [18] Jia Li, Lu Wang, Lei Zhang, and Beibei Wang. TensoSDF: Roughness-aware tensorial representation for robust geometry and material reconstruction. *ACM TOG*, 2024. 2, 6
- [19] Zhaoshuo Li, Thomas Müller, Alex Evans, Russell H Taylor, Mathias Unberath, Ming-Yu Liu, and Chen-Hsuan Lin. Neuralangelo: High-fidelity neural surface reconstruction. In *CVPR*, 2023. 2
- [20] Zhihao Liang, Qi Zhang, Ying Feng, Ying Shan, and Kui Jia. GS-IR: 3d gaussian splatting for inverse rendering. In *CVPR*, 2024. 2, 6
- [21] Yuan Liu, Peng Wang, Cheng Lin, Xiaoxiao Long, Jiepeng Wang, Lingjie Liu, Taku Komura, and Wenping Wang. NeRO: Neural geometry and brdf reconstruction of reflective objects from multiview images. *ACM TOG*, 2023. 2, 6, 8
- [22] Joakim Löw, Joel Kronander, Anders Ynnerman, and Jonas Unger. BRDF models for accurate and efficient rendering of glossy surfaces. *ACM TOG*, 2012. 1
- [23] Ben Mildenhall, Pratul P Srinivasan, Matthew Tancik, Jonathan T Barron, Ravi Ramamoorthi, and Ren Ng. NeRF: Representing scenes as neural radiance fields for view synthesis. In *ECCV*, 2020. 1, 2

[24] Nicolas Moenne-Loccoz, Ashkan Mirzaei, Or Perel, Riccardo de Lutio, Janick Martinez Esturo, Gavriel State, Sanja Fidler, Nicholas Sharp, and Zan Gojcic. 3d gaussian ray tracing: Fast tracing of particle scenes. *ACM TOG*, 2024. 2

[25] Claus Müller. *Spherical harmonics*. 2006. 4

[26] Thomas Müller, Alex Evans, Christoph Schied, and Alexander Keller. Instant neural graphics primitives with a multiresolution hash encoding. *ACM TOG*, 2022. 1, 2

[27] Addy Ngan, Frédéric Durand, and Wojciech Matusik. Experimental analysis of BRDF models. *Rendering Techniques*, 2005. 1

[28] Michael Oechsle, Songyou Peng, and Andreas Geiger. UNISURF: Unifying neural implicit surfaces and radiance fields for multi-view reconstruction. In *ICCV*, 2021. 2

[29] OpenAI. Gpt-4o system card. <https://openai.com/index/gpt-4o-system-card>, 2024. 11, 12

[30] Taesung Park, Alexei A Efros, Richard Zhang, and Jun-Yan Zhu. Contrastive learning for unpaired image-to-image translation. In *ECCV*, 2020. 2

[31] Poly Haven. Poly haven: The public 3d asset library. <https://polyhaven.com/>, 2025. 3, 11

[32] Zhenxiong Tan, Songhua Liu, Xingyi Yang, Qiaochu Xue, and Xinchao Wang. Ominicontrol: Minimal and universal control for diffusion transformer. In *ICCV*, 2025. 2, 3, 5

[33] Jingguang Tong, Xuesong Li, Fahira Afzal Maken, Sundaram Muthu, Lars Petersson, Chuong Nguyen, and Hongdong Li. GS-2DGS: Geometrically supervised 2dgs for reflective object reconstruction. In *CVPR*, 2025. 2, 6

[34] Dor Verbin, Peter Hedman, Ben Mildenhall, Todd Zickler, Jonathan T Barron, and Pratul P Srinivasan. Ref-nerf: Structured view-dependent appearance for neural radiance fields. *IEEE TPAMI*, 2024. 6, 7, 8

[35] Dor Verbin, Pratul P Srinivasan, Peter Hedman, Ben Mildenhall, Benjamin Attal, Richard Szeliski, and Jonathan T Barron. Nerf-casting: Improved view-dependent appearance with consistent reflections. In *SIGGRAPH Asia*, 2024. 2

[36] Bruce Walter, Stephen R Marschner, Hongsong Li, and Kenneth E Torrance. Microfacet models for refraction through rough surfaces. *Rendering Techniques*, 2007. 4

[37] Peng Wang, Lingjie Liu, Yuan Liu, Christian Theobalt, Taku Komura, and Wenping Wang. NeuS: learning neural implicit surfaces by volume rendering for multi-view reconstruction. In *NeurIPS*, 2021. 1

[38] Yiming Wang, Qin Han, Marc Habermann, Kostas Daniilidis, Christian Theobalt, and Lingjie Liu. NeuS2: Fast learning of neural implicit surfaces for multi-view reconstruction. In *ICCV*, 2023. 2

[39] Chenfei Wu, Jiahao Li, Jingren Zhou, Junyang Lin, Kaiyuan Gao, Kun Yan, Sheng-ming Yin, Shuai Bai, Xiao Xu, Yilei Chen, et al. Qwen-image technical report. *arXiv preprint arXiv:2508.02324*, 2025. 7

[40] Yuxuan Yao, Zixuan Zeng, Chun Gu, Xiatian Zhu, and Li Zhang. Reflective gaussian splatting. In *ICLR*, 2025. 1, 2, 4, 6, 12

[41] Lior Yariv, Jiatao Gu, Yoni Kasten, and Yaron Lipman. Volume rendering of neural implicit surfaces. In *NeurIPS*, 2021. 1, 2

[42] Zehao Yu, Songyou Peng, Michael Niemeyer, Torsten Satler, and Andreas Geiger. MonoSDF: Exploring monocular geometric cues for neural implicit surface reconstruction. *NeurIPS*, 2022. 2

[43] Youjia Zhang, Anpei Chen, Yumin Wan, Zikai Song, Junqing Yu, Yawei Luo, and Wei Yang. Ref-GS: Directional factorization for 2d gaussian splatting. In *CVPR*, 2025. 2, 6, 12

[44] Jun-Yan Zhu, Taesung Park, Phillip Isola, and Alexei A Efros. Unpaired image-to-image translation using cycle-consistent adversarial networks. In *ICCV*, 2017. 2

# Pygmalion Effect in Vision: Image-to-Clay Translation for Reflective Geometry Reconstruction

## Supplementary Material

### A.1. Analogy to the Pygmalion effect

The Pygmalion effect, originally a psychological phenomenon describing how expectations can shape outcomes, finds an intriguing parallel in our study. In the myth, the sculptor *Pygmalion* creates a statue so lifelike that his belief in its beauty brings it to life. Similarly, our model is trained on datasets curated through the expectations of “what a correct reflective object should look like.” These expectations, embedded in the proposed image-to-clay translation, recursively reinforce the model’s perception of the object.

In our work, this metaphor captures the essence of geometry-aware generative reconstruction: our learning framework not only reconstructs the observed world but also projects the internal geometric belief of the image-to-clay translation model back into the image domain, closing a loop between seeing and shaping. By acknowledging this Pygmalion effect in vision, we emphasize the importance of critical evaluation, ensuring that the visual worlds our models bring to life remain faithful to reality rather than to their own internal expectations through evaluation benchmarks.

### A.2. Data preparation for image-to-clay model

**Objaverse-rendered dataset.** To construct the training dataset for the image-to-clay translation model, we used the Objaverse dataset [4, 5] and generated paired renderings by manipulating material properties under diverse lighting conditions. Specifically, we rendered using 70 environment maps from PolyHaven [31] to ensure realistic and varied illumination. The material parameters were adjusted by varying the metalness value  $m$  and roughness  $r$ . The roughness was resampled for all samples from a uniform distribution  $r \sim \mathcal{U}(0.03, 0.3)$ . For the metalness, 70% of the samples were rendered as metallic by setting  $m = 1$ , while the remaining 30% retained their original metallic values.

When generating objects with clay materials, we set  $m = 0$  and  $r = 1$  to emulate diffuse, non-reflective surfaces. To cover both background-removed and non-removed cases, approximately 30% of the rendered images had their backgrounds removed.

**Model-generated dataset.** To generate more realistic image pairs, we generate clay-like images using FLUX, and then transform them into reflective objects using Nano-Banana. The reasons we choose this approach instead of generating images first and then converting them into clay-like images are twofold. First, when using Nano-Banana to convert images into clay-like images, shape distortions



Figure A1. Ablation study illustrating the impact of model-generated dataset construction order. When reflective images are generated first and then transformed into clay, the model tends to produce more variations in fine details.

occurred more frequently, as shown in Fig. A1. Second, Nano-Banana produces more realistic environment-map reflections compared to FLUX, allowing us to generate more realistic and challenging data that is beneficial for model training.

To create a diverse set of clay-like images, we used ChatGPT-4o [29] to generate 5,000 prompts based on the instruction in Tab. A1, which requires white-plaster objects, non-white colored backgrounds, and random sampling of 1–3 objects and background scenes. For the clay-to-image transformation, we define 12 reflective material categories and uniformly sample one material per image to produce the reflective prompts described in Tab. A1.

### A.3. Detailed formulation of 2D Gaussian Splatting

2D Gaussian Splatting (2DGS) [9] improves upon Gaussian-based representations by defining oriented 2D disks instead of volumetric Gaussians. Each Gaussian is represented on a local tangent plane, parameterized by its center  $\mathbf{p}$ , two tangential directions  $\mathbf{t}_u, \mathbf{t}_v$ , and scaling factors  $s_u, s_v$ . A surface point on the disk is expressed as:

$$\mathbf{P}(u, v) = \mathbf{p} + s_u \mathbf{t}_u u + s_v \mathbf{t}_v v. \quad (12)$$

The Gaussian weight over this plane is:

$$\mathcal{G}(u, v) = \exp\left(-\frac{u^2 + v^2}{2}\right). \quad (13)$$

During rendering, a pixel  $\mathbf{x}$  is projected onto the local plane of each Gaussian, yielding the corresponding local coordi-

Category	Component	Content
Clay-like image generation	Instruction	<i>Generate prompts under the following rules: The object(s) must appear in white plaster material, but the background must not be white. The scene should contain 1 to 3 objects. Objects should be randomly selected (e.g., chair, vase, tumbler, laptop, tools). Backgrounds should also be randomly selected (e.g., indoor room, city street, forest path, brick pavement).</i>
	Example prompts	<i>A pair of white plaster clay models: dice and a folded tent, placed on a gray stone pavement with a neon wall behind.</i> <i>A single white plaster clay drawer chest placed upon a smooth concrete floor, with no background details visible.</i> <i>Two white plaster clay objects—a hockey stick and a stapler—arranged on a light wooden floor with no background details.</i>
Image-to-clay transformation	Prompt template	<i>Change the surface material of the white clay object in this picture to reflective and polished {material}, preserving the exact shape, geometry, and all fine-grained irregularities without modifying any background region. The new surface must accurately reflect the surrounding environment.</i>
	{material} options	<i>painted metal, ceramic, brass, iron, gold, chrome, dark colored ceramic, glossy plastic, stone, brushed metal, metallic material, glossy material</i>

Table A1. Prompts for constructing clay–image paired data were generated using FLUX [16] and Nano-Banana [7]. To create complex prompts that produce diverse objects, we used ChatGPT-4o [29] with the specified instruction. Finally, prompts created with the template and selected materials were used to convert clay objects into reflective objects using Nano-Banana.

nates  $\mathbf{u}(\mathbf{x}) = [u(\mathbf{x}), v(\mathbf{x})]^\top$  through the inverse projection of  $\mathbf{P}(u, v)$ . The color at  $\mathbf{x}$  is then obtained by the standard alpha-compositing rule:

$$\mathbf{c}(\mathbf{x}) = \sum_{i=1}^N \mathbf{c}_i \alpha_i \hat{\mathcal{G}}_i(\mathbf{u}(\mathbf{x})) \prod_{j=1}^{i-1} \left(1 - \alpha_j \hat{\mathcal{G}}_j(\mathbf{u}(\mathbf{x}))\right), \quad (14)$$

where  $\mathbf{c}_i$  is the Gaussian color,  $\alpha$  is the Gaussian opacity, and  $\hat{\mathcal{G}}$  is the visibility-corrected Gaussian weight of  $\mathcal{G}$ .

#### A.4. Additional implementation details

For fine-tuning OminiControl, we adopt the spatially aligned conditioning configuration from the original implementation, including its learning rate, LoRA hyperparameters, and other training settings. All transformed images are rendered at a fixed resolution of 512×512. The model is trained for 100,000 iterations using eight H100 GPUs with a batch size of 8, and a simple cropping-based image augmentation is applied during training.

For the reflective object reconstruction stage, we use a single H100 GPU for both the image-to-clay transformation and Gaussian splatting training. For the GlossySynthetic and Shiny Blender datasets, we follow Ref-GS [43] and RGS [40] and remove the background using the provided masks. When masks are available, we also apply the mask loss from R3DG [6] to improve training stability.

For DTU, we follow the training configuration of 2DGS [9], retaining the background in the RGB reconstruction branch as in the original setup. To prevent the image-to-clay model from modifying background regions, however,

we apply the DTU masks only when replacing the foreground with its clay counterpart. For Ref-Real, where no masks are provided, the full clay image is used.

We train the reconstruction model for 50,000 iterations, using clay-branch regularization for the first 10,000 iterations and RGB-only supervision thereafter. A few scenes in GlossySynthetic (Tbell, Teapot, and Bell) fall back to baseline-like behavior once clay supervision is removed, so we use only the clay-supervised stage and stop training these scenes at 10,000 iterations. For the Cat scene, we delay the smooth normal loss to maintain fine geometric details, as done in the original 2DGS [9] setup. For Ref-Real scenes, we train the model for 20,000 iterations following RGS [40].

#### A.5. Additional visualization and results

In this section, we provide additional visualizations of the image-to-clay transformation results and our reconstructed outputs. Figs. A2 and A3 present samples from the datasets used to train our image-to-clay model. Fig. A2 contains data generated from Objaverse, while Fig. A3 shows data constructed using FLUX and Nano-Banana. The results produced by the model trained on these datasets are shown in Fig. A4. Fig. A5 visualizes various BRDF parameters learned for rendering. Fig. A6 further presents additional normal maps and RGB outputs. Even when the RGB outputs appear similar, the normal maps demonstrate that our method learns sharper boundaries and more accurate geometric details compared to existing approaches.



Figure A2. Examples of the Objaverse-based image–clay paired dataset. The top row shows reflective renderings of the objects. The bottom row shows the same objects rendered with clay-like material properties.



Figure A3. Examples of model-based image-clay paired dataset generated by FLUX and Nano-Banana. The top row shows reflective object images converted by Nano-Banana from FLUX-generated clay images. The bottom row shows the clay-like images generated by FLUX.



Figure A4. Samples of images converted by our image-to-clay model. The top row shows the input images, and the bottom row shows the resulting clay images.

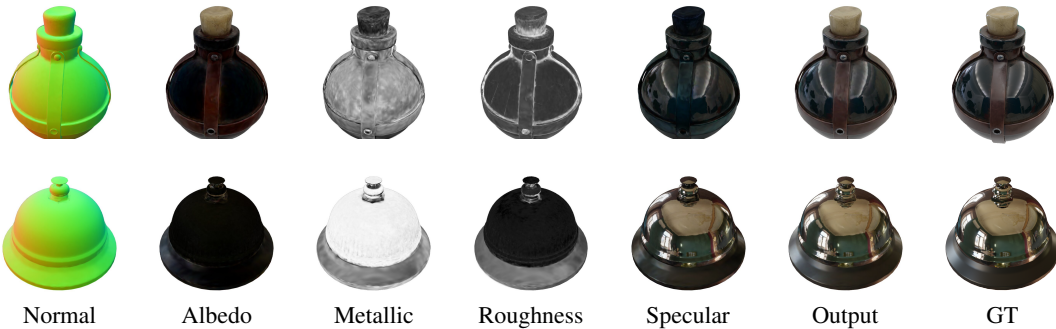


Figure A5. Visualization of the decomposed material parameters on the Glossy Synthetic Dataset. The top row shows the results for Potion, and the bottom row shows the results for Tbell.

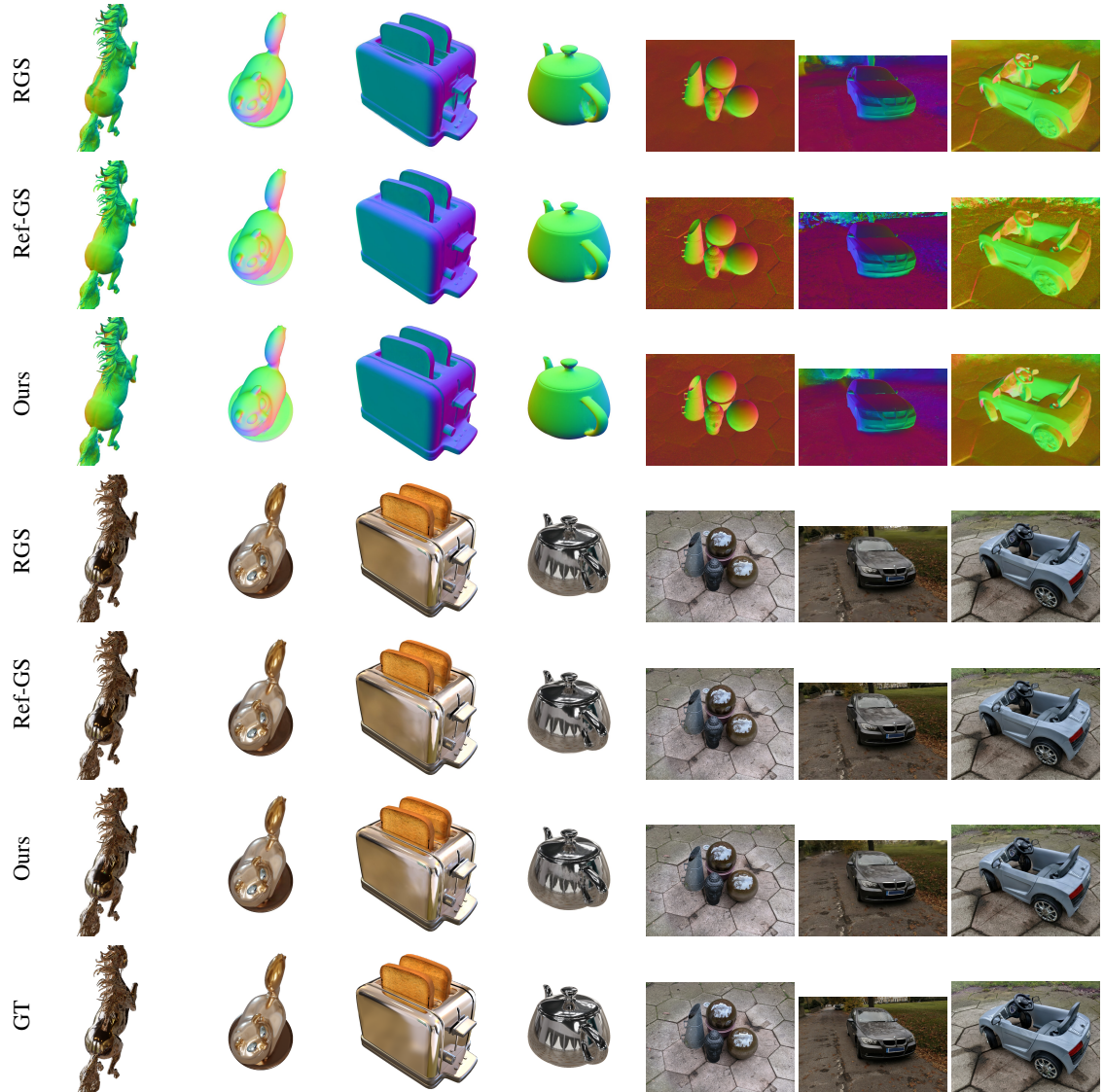


Figure A6. Additional visualization results for reflective object reconstruction. Rows 1–3 show the estimated normal maps, rows 4–6 present the RGB outputs, and row 7 shows the ground truth. Even when the RGB outputs appear similar, our method learns sharper boundaries and more accurate geometric details compared to existing approaches.